

Static Recrystallization Simulation of Interstitial Free-Steel by Coupling Multi-Phase-Field and Crystal Plasticity Model Considering Dislocation Density Distribution

Alireza Rezvani, Ramin Ebrahimi,* and Ebad Bagherpour*

Knowledge of alloy recrystallization is key to optimizing microstructures and achieving superior material properties. Computational models predicting microstructural evolution during recrystallization significantly enhance control of microstructure formation during manufacturing. Accurate prediction of microstructural parameters, including recrystallization fraction and grain size, is highly desirable. However, developing robust recrystallization models under various processing conditions remains an active research area. Herein, using interstitial free-steel for simulations and experiments, plastic deformation of polycrystalline material is simulated using a physics-based crystal plasticity model. A real microstructure serves as the initial configuration. The resulting inhomogeneous dislocation density distribution and deformed grain topology are used in a multi-phase-field simulation of recrystallization. In primary recrystallization, nucleation strongly influences kinetics and the final microstructure. In the model, the dislocation density distribution predicts both the number and positions of nuclei. Comparing simulations—one considering the dislocation density distribution in both nucleation and evolution and the other assuming constant dislocation density and random seed positioning—demonstrates the importance of heterogeneous dislocation distribution. Results confirm that static recrystallization simulations, accurately reflecting plastic deformation and utilizing the dislocation density distribution as the driving force for grain growth and nucleation, can be successfully performed using the proposed model.

1. Introduction

The microstructure established during the cold working process serves as a critical foundation for the static recrystallization (SRX) phenomenon that occurs during annealing process. The characteristics of this initial microstructure, including grain size, dislocation density, and texture, profoundly impact the kinetics and final grain structure of the recrystallized material.^[1]

Thermomechanical processing (TMP) routes, which can induce recrystallization, are essential for tailoring the microstructure of alloys to achieve specific properties in final products. To optimize these properties, a comprehensive understanding, control, and prediction of recrystallization is paramount.^[2,3] This necessitates a combination of experimental and computational approaches. A computational model capable of accurately predicting microstructural evolution during recrystallization would significantly enhance our ability to control microstructure formation during TMP.

The manufacturing industry demands accurate prediction of fundamental microstructural parameters, including recrystallization fraction and grain size, under real-world processing conditions.^[4] Current models, however, exhibit limited accuracy due to an incomplete representation of the deformed microstructure.

To achieve precise numerical predictions of microstructure and texture evolution during SRX, it is crucial to integrate a comprehensive representation of the deformation microstructure, including inhomogeneities, within the SRX simulation model. A coupled crystal plasticity-microstructure evolution model is considered the most promising approach for designing SRX microstructures.^[5,6]

Prior work has demonstrated the coupling of phase-field models of recrystallization with other simulation methods. For instance, Takaki et al.^[7–9] linked recrystallization simulations to crystal plasticity models, successfully simulating recrystallized grain growth considering heterogeneous plastic deformation. However, their simulated final SRX microstructure strongly depended on the employed nucleation criteria and was limited to a small number of deformed grains. Similarly, Vondrous et al.^[10] employed a coupled crystal plasticity and phase-field

A. Rezvani, R. Ebrahimi
Department of Materials Science and Engineering
School of Engineering
Shiraz University
7134851154 Shiraz, Iran
E-mail: ebrahimi@shirazu.ac.ir

E. Bagherpour
Brunel Centre for Advanced Solidification Technology (BCAST)
Brunel University of London
Uxbridge UB8 3PH, UK
E-mail: Ebad.Bagherpour@Brunel.ac.uk

 The ORCID identification number(s) for the author(s) of this article can be found under <https://doi.org/10.1002/adem.202500117>.

© 2025 The Author(s). Advanced Engineering Materials published by Wiley-VCH GmbH. This is an open access article under the terms of the Creative Commons Attribution License, which permits use, distribution and reproduction in any medium, provided the original work is properly cited.

DOI: 10.1002/adem.202500117

approach to analyze grain structure evolution during annealing in sheet metal production of low carbon steel. Min et al. utilized a similar coupling to predict recrystallization in ultralow carbon^[11] and electrical steels.^[12] Luan et al.^[13] also used the same combination to investigate SRX in pure aluminum. Roy et al.^[14] utilized the same methodology to simulate SRX and grain growth during hot-forming in Ti-alloys. Notably, these studies utilized synthetic representative volume elements (RVEs) as initial microstructures, characterized by a limited grain count and planar grain boundaries. This simplification neglects the inherent curvature observed in experimental samples, potentially impacting the accuracy of predicted microstructure evolution during subsequent deformation and recrystallization processes.

Beyond phase-field approaches, alternative simulation techniques have also been coupled with crystal plasticity. For example, Raabe et al.^[15,16] developed a crystal plasticity-finite element (CP-FE) and cellular automaton model to simulate primary SRX microstructure evolution. Likewise, Radhakrishnan et al.^[17,18] presented SRX models coupling CP-FE with Monte Carlo techniques.

In these models, the stored energy calculated from the dislocation density, simulated by CP-FE, serves as the driving force for recrystallized grain growth. While these models successfully simulate recrystallized grain growth considering heterogeneous plastic deformation, the final SRX microstructure and texture are strongly influenced by the employed nucleation criteria. Therefore, developing accurate nucleation criteria for recrystallized grains remains a significant challenge.

While other authors successfully captured recrystallized microstructures by incorporating heterogeneous plastic deformation into their simulations, the final SRX microstructures were highly sensitive to the accuracy of nucleation modeling. Additionally, the nonuniform distribution of stored energy within the material significantly influences the kinetics of SRX. This energy heterogeneity directly affects the nucleation and growth of recrystallized grains, leading to variations in the final grain size and shape distribution within the material's microstructure.^[19,20]

Given the critical role of nucleation and growth in determining the final microstructure of recrystallized materials, establishing accurate nucleation criteria and growth model for recrystallized grains constitutes a substantial challenge that requires further investigation.

In this article, a physics-based crystal plasticity model implemented in the open-source software DAMASK^[21–23] is used for predicting the deformed microstructure and total dislocation distribution coupled with the multi-phase-field (MPF) model proposed by Fan and Chen^[24–27] for the microstructural evolution simulation. Both simulations along with the experimental investigations were performed on interstitial free (IFN) steel samples. This study introduces a novel approach to SRX modeling by directly linking nucleation site prediction to dislocation density evolution, eliminating the need for empirical assumptions. Unlike prior studies that rely on experimentally derived grain counts or preassigned nucleation distributions, our method predicts nucleation directly from dislocation accumulation, ensuring a physically consistent representation of recrystallization initiation. Additionally, we employ optical microscopy to generate initial microstructures instead of relying on synthetic or

small-scale eModel. Simul. Mater. Sci. Eng. lectron backscatter diffraction (EBSD)-based datasets. This enables larger-scale simulations that are more representative of industrial processing while remaining cost-effective and widely accessible. Furthermore, we integrate an in-house computational framework that automates the extraction of microstructural features from experimental optical microscopy images and converts them to a readable format for crystal plasticity modelling. In the coupling process between crystal plasticity and phase-field models, a grid refinement process was performed using an interpolation algorithm. This minimized grain area alterations after conversion from a sharp to a diffuse interface, while ensuring continuity in the dislocation density field. The refined computational grid ensures that the characteristic length scale of the diffuse interface remains well below the minimum grain size, preventing unintended dissolution of small grains, ensuring consistency across different stages of the simulation. By combining these advancements, our approach enhances the accuracy, scalability, and predictive capability of recrystallization modeling, making it more adaptable for studying different materials and processing conditions. To validate our model, hardness testing was performed to derive Avrami parameters and an in-house image processing tool was developed for quantitative grain size analysis. The strong agreement between experimental and simulated results supports the robustness of the model in predicting recrystallization kinetics and microstructural evolution.

2. Experimental Section

The SRX simulation employed in this research consists of four sequential stages: 1) Microstructural Characterization: A custom-developed image analysis code is employed to extract the grains distribution from the optical microscopy images of the as-received microstructure. This data is then used to generate a RVE that serves as the initial microstructure for subsequent crystal plasticity simulation. 2) Crystal Plasticity Modeling: A crystal plasticity model is utilized to predict the deformed microstructure resulting from cold work deformation. 3) Model Coupling: The integration of crystal plasticity and phase-field models, performed after the crystal plasticity simulation stage, allows for a comprehensive simulation of the recrystallization process by considering the final microstructure of the crystal plasticity model, as initial microstructure for the phase-field model. 4) Phase-Field Modeling: A phase-field model is utilized to simulate the SRX process. This model tracks the evolution of grain boundaries and the growth of recrystallized grains during the annealing process.

The proposed simulation procedure is summarized in a flow chart as shown in **Figure 1**. Detailed descriptions of each stage are provided in the subsequent sections.

2.1. Microstructural Characterization

The material employed in this study is a commercial IFN steel with a chemical composition determined by quantitative analysis and presented in **Table 1**. The IFN steel, owing to its chemical composition, exhibited a stable body-centered cubic (BCC) crystal structure throughout the processing conditions employed,

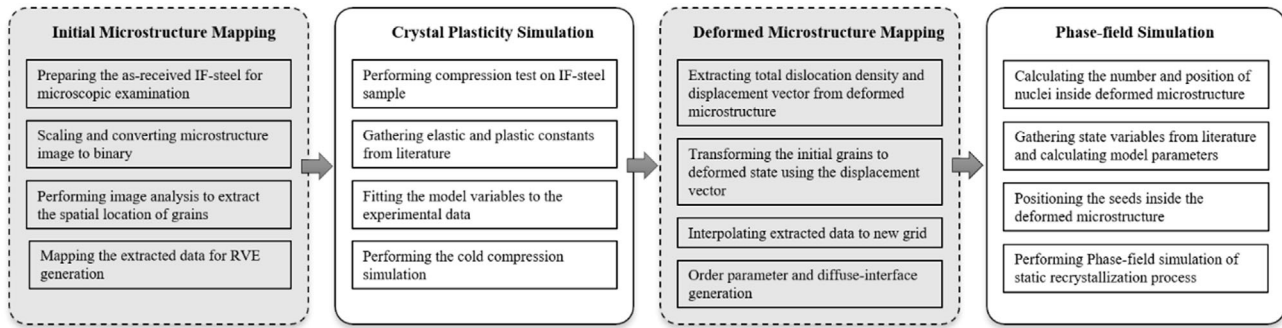


Figure 1. Overall flow chart of the simulation procedure for the integrated coupled crystal plasticity and phase-field model.

Table 1. Chemical composition of the IFN steel used in this study (Wt. (%)).

C	Si	Mn	P	S	N	Al	Cr	Mo	Ni	Nb	V	Ti
0.002	0.020	0.13	0.005	0.009	0.0032	0.030	0.037	0.008	0.025	0.002	0.002	0.062

including cold compression, annealing, and water quenching, thereby excluding phase transformation effects from the analysis. This allowed for a clear evaluation of SRX mechanisms without interference from transformation-induced recrystallization.

The initial microstructure was analyzed using optical microscopy and is shown in **Figure 2a** with Nital 2% etchant. A homogeneous, single-phase microstructure was observed, containing 238 grains with a mean grain size of 40 μm . A custom MATLAB code was developed to perform microstructural analysis (after transforming the original image to binary image), including grain identification and indexing. The results of this analysis are shown in **Figure 2b**, where each grain is individually indexed and color-coded on the micrograph.

Grain boundaries were eliminated by expanding nearest neighboring grains in the microstructure and converted to a readable format for subsequent analysis in the Dream.3D software package.^[28] The crystallographic orientation of each grain

was assigned according to a random texture, and the final microstructure was exported in a format compatible with the preprocessor of the DAMASK crystal plasticity simulation package for the creation of the initial geometry and material files.

To ensure accurate representation of the microstructure in the DAMASK simulations, it is crucial to carefully consider the scale and resolution when converting the original microstructure image. The inverse pole figure (IPF) color map of the resultant microstructure, as shown in **Figure 3**, is a grid of 700 \times 700 points.

In the cold working process, cylindrical specimens, machined from the as-received material using wire electrical discharge machining to a diameter of 10 mm and a height of 15 mm, were subjected to a compression test to induce a true strain of 0.45.

Subsequently, a heat treatment process was conducted at 750 $^{\circ}\text{C}$, followed by quenching in cold water. The normal plane of the specimens was meticulously prepared through grinding,

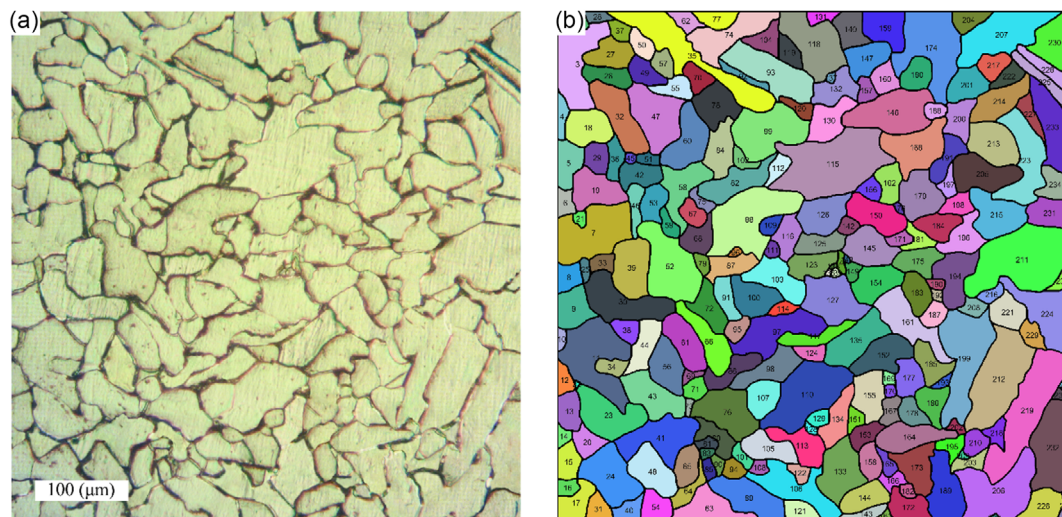


Figure 2. Microstructure of as-received IFN steel: a) original image; b) digitized and indexed.

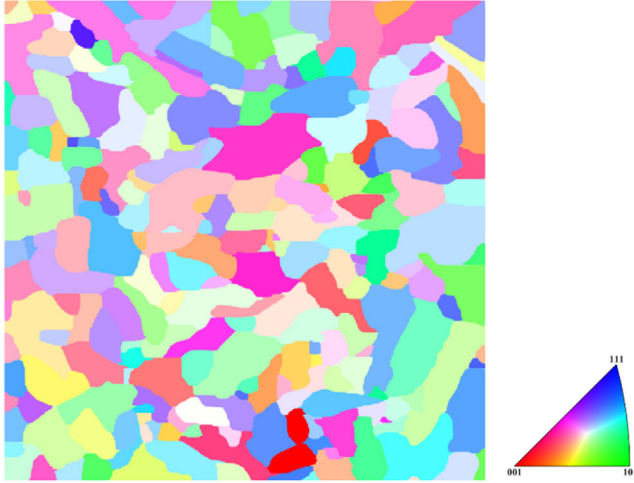


Figure 3. Initial grain structure (IPF color map) used in crystal plasticity simulation.

polishing, and etching after annealing for durations of 0, 1, 2, 3, 4, and 5 min. Optical microscopy was employed to investigate the extent of recrystallization by analyzing the microstructural evolution.

2.2. Crystal Plasticity Model

Crystal plasticity models offer the capability to simulate the activation of individual slip systems and account for the influence of grain orientation on slip inhibition. This enables the prediction of full-field, heterogeneous strain and dislocation density distributions within a polycrystalline microstructure.

Given the objective of this paper, which is to incorporate non-uniform dislocation density distributions into phase-field modeling, a physics-based crystal plasticity model is a suitable choice. Consequently, the cold-work deformation simulations were conducted using a physics-based crystal plasticity model implemented within the open-source software DAMASK. The subsequent section delves into the constitutive law employed in these simulations.

The constitutive model employed in this study is based on the dislocation density approach proposed by Ma and Roters.^[29,30] This framework directly accounts for the fundamental mechanisms of dislocation multiplication, annihilation, and dipole formation.

The shear rate on a slip system, α , $\dot{\gamma}^\alpha$, is directly linked to the average velocity of mobile dislocations, v^α . This relationship is described by the Orowan equation,^[31] which states that

$$\dot{\gamma}^\alpha = \rho^\alpha b v^\alpha \quad (1)$$

where ρ^α is the mobile dislocation density of the slip system α and b is the magnitude of the burgers vector.

The distance between short-range barriers and the average activation energy for overcoming these barriers are the main factors controlling dislocation velocity,^[32,33] which is given as

$$v^\alpha = \frac{l}{t_w + t_r} \quad (2)$$

where l denotes the average distance between the short-range barriers, t_w is the time a dislocation spends waiting to overcome a barrier, while t_r represents the time it takes to move between barriers. Given that t_r is significantly shorter than t_w , the waiting time is often considered to be the dominant factor and the running time is neglected.^[32] In accordance with the model of Kocks et al.^[34] the waiting time is calculated as

$$t_w = \omega_0^{-1} \exp\left(\frac{\Delta G}{k_B T}\right) \quad (3)$$

where ΔG is the average activation energy, ω_0 is the attempt frequency, T is the absolute temperature, and k_B is Boltzmann's constant. The dislocation glide velocity is evaluated using Equation (2) and (3) as

$$v^\alpha = v_0 \exp\left(\frac{-\Delta G}{k_B T}\right) \quad (4)$$

$$v_0 = l \omega_0 \quad (5)$$

Inserting Equation (4) into 1 gives the shear rate as

$$\dot{\gamma}^\alpha = \rho^\alpha b v_0 \exp\left(\frac{-\Delta G}{k_B T}\right) \quad (6)$$

The stress dependency of ΔG can be expressed as

$$\Delta G = \Delta F \left[1 - \left(\frac{\tau_T^{*\alpha}}{\tau_0^{*\alpha}} \right)^p \right]^q \quad (7)$$

where ΔF represents the total short-range barrier energy, that is, the activation energy for glide in the absence of external stress. The shape of the short-range barrier is characterized by parameters p and q , which, for most barrier profiles, satisfy the conditions $0 < p \leq 1$ and $1 \leq q \leq 2$.^[34] The thermal stress component, $\tau_T^{*\alpha}$, is determined by

$$\tau_T^{*\alpha} = \begin{cases} |\tau^\alpha| - \tau_G^\alpha & \text{for } |\tau^\alpha| > \tau_G^\alpha \\ 0 & \text{for } |\tau^\alpha| \leq \tau_G^\alpha \end{cases} \quad (8)$$

where τ_α denotes the total resolved shear stress acting on slip system α , while τ_G^α represents the athermal component of the resolved shear stress, which is defined as

$$\tau_G^\alpha = Gb \left(\sum_{\alpha'=1}^{N_s} \xi_{\alpha\alpha'} (\rho^\alpha + \rho^{\alpha'}) \right)^{1/2} \quad (9)$$

where ρ_d^α is the dislocation dipole density, $\xi_{\alpha\alpha'}$ is the interaction coefficient matrix between different slip systems α and α' , G is the shear modulus, and τ_0^* is the barrier strength, the stress needed to overcome short-range barriers without thermal assistance, which is given as

$$\tau_0^* = (|\tau^\alpha| - \tau_G^\alpha) \text{ at } T = 0K \quad (10)$$

By combining Equation (6) and (7), the shear rate for slip system α is obtained as follows

$$\dot{\gamma}^\alpha = \rho^\alpha b v_0 \exp \left[-\frac{\Delta F}{k_B T} \left(1 - \left(\frac{\tau^* \alpha}{\tau_0^*} \right)^p \right)^q \right] \text{sign}(\tau^\alpha) \quad (11)$$

The evolution rate of the mobile dislocation density and the dislocation dipole density are given as^[22,35]

$$\dot{\rho}^\alpha = \frac{|\dot{\gamma}^\alpha|}{b \Lambda^\alpha} - \frac{2d_{\text{dipole}}^\alpha}{b} \rho^\alpha |\dot{\gamma}^\alpha| \quad (12)$$

$$\dot{\rho}_d^\alpha = \frac{2(d_{\text{dipole}}^\alpha - d_{\text{anni}}^\alpha)}{b} \rho^\alpha |\dot{\gamma}^\alpha| - \frac{2d_{\text{anni}}^\alpha}{b} \rho_d^\alpha |\dot{\gamma}^\alpha| \quad (13)$$

where d_{anni}^α represents the critical distance required for the annihilation of two mobile dislocations of opposite sign. The annihilation term in the Equation (12), is calculated under the assumption of equal populations of positive and negative dislocations. The dislocation mean free path, Λ^α ,^[22] is determined by

$$\frac{1}{\Lambda^\alpha} = \frac{1}{d_g} + \frac{1}{\lambda^\alpha} \quad (14)$$

where d_g is the effective grain size and $\frac{1}{\lambda^\alpha}$ is defined as

$$\frac{1}{\lambda^\alpha} = \frac{1}{C_\lambda} \left(\sum_{\alpha'=1}^{N_s} g_{\alpha\alpha'} (\rho^{\alpha'} + \rho_d^{\alpha'}) \right)^{1/2} \quad (15)$$

where C_λ is a coefficient that characterizes the number of dislocations that can traverse a given distance before becoming immobilized by forest dislocations. The coefficients $g_{\alpha\alpha'}$ represent the interactions between dislocations on different slip systems.

Finally, the critical distance for dipole formation is expressed as

$$d_{\text{dipole}}^\alpha = \frac{G}{16\pi|\tau^\alpha|} b \quad (16)$$

The crystal plasticity simulation, employing the presented constitutive law, was performed using the spectral solver implemented in DAMASK. A compressive loading condition was applied to achieve an average strain of 0.45. Accurate material parameter selection is crucial for crystal plasticity models to reliably predict a material's deformation behavior. While single-crystal experiments offer a pathway to determine many material parameters for physics-based crystal plasticity models, macroscopic experiments, such as uniaxial compression tests, are more practical for polycrystalline engineering materials. The model parameters are adjusted (Table 2) to achieve optimal agreement with the experimental macroscopic stress–strain response using a series of simulations (Figure 4) and made sure that the parameters are in the range specified for DAMASK simulation kit.^[36,37] Notably, detailed analyses of slip systems and hardening parameters are well-documented for IF steel within the DAMASK framework,^[36,37] providing a robust foundation for our parameter selection. The remaining properties, including the Burgers

Table 2. Optimized constitutive parameters for DAMASK simulation.

ρ_0^α [m^{-2}]	ν_0 [ms^{-1}]	ΔF [J]	τ_0^* [MPa]	p	q	C_λ	C_{anni}
2.8×10^{12}	1.01×10^3	1.7×10^{-19}	450	0.46	1.4	25.4	707

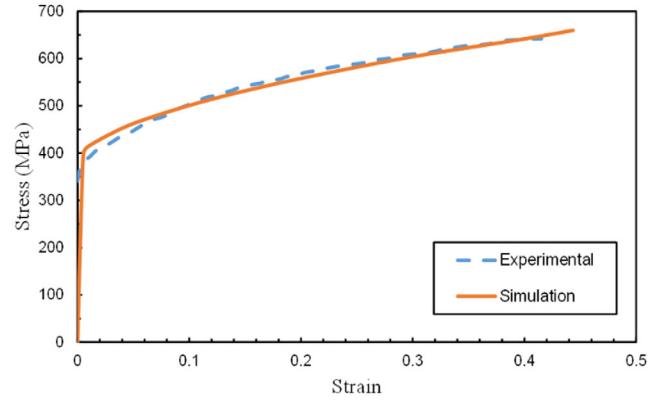


Figure 4. Experimental and simulated true stress–strain response of IFN steel in compression.

vector magnitude, b , and shear modulus, G , were acquired from existing literature on IFN steel.

2.3. Model Coupling

The final microstructure from the crystal plasticity model is used as the initial condition for the phase-field simulation. To extract grain boundaries and individual grains, the initial grain configuration is deformed using the displacement vectors calculated during the crystal plasticity simulation. Subsequently, the indices of each grain and the total dislocation density at every point are extracted and imported into a MATLAB code for further processing.

It should be pointed out that the phase-field method is a diffuse-interface method, meaning that grain boundaries have a finite width.^[38] Therefore, a sufficiently fine grid spacing is required to accurately represent the microstructure. Additionally, the insertion of nuclei demands a small enough grid size to correctly capture their topology, as nuclei are typically smaller than the overall microstructure. Taking the previous consideration into account, the coupling algorithm interpolates the grain and dislocation density data according to the new increased grid size. Additionally, the scale of the microstructure was carefully adjusted to align with the new grid size, which is essential for accurate phase-field simulations.

2.4. MPF Method

The total free energy of an inhomogeneous system is written in terms of all orientation field variables and their gradients, F_{bulk} and F_{int} ,^[25] respectively, plus the stored energy field,^[39,40] F_s , due to plastic deformation. Thus, the total free energy function is given as

$$\begin{aligned} \mathcal{F} &= F_{\text{bulk}} + F_{\text{int}} + F_s \\ &= \int_V [f_{\text{bulk}}(\{\eta_i\}) + f_{\text{int}}(\{\eta_i\}, \{\nabla \eta_i\}) + f_s(\{\eta_i\})] dV \end{aligned} \quad (17)$$

where V is the volume of the system, η_i ($i = 1, \dots, g$) are called orientation field variables^[38] for distinguishing different grains in the microstructure and g is the total number of grains.

The bulk energy provides potential wells with equal depth at $(\eta_1, \dots, \eta_g) = (1, 0, \dots, 0), \dots, (0, 0, \dots, 1)$ which provides the driving force for grains to fill the simulation domain. The gradient energy density is nonzero only around the grain boundaries.^[41]

$$f_{\text{bulk}} + f_{\text{int}} = m_0 \left[\sum_{i=1}^g \left(\frac{\eta_i^4}{4} - \frac{\eta_i^2}{2} \right) + \gamma \sum_{i=1}^g \sum_{j>i}^g \eta_i^2 \eta_j^2 + \frac{1}{4} \right] + \frac{\kappa}{2} \sum_{i=1}^g |\nabla \eta_i|^2 \quad (18)$$

where m_0 is the energy density coefficient and γ is a positive constant equal to 1.5 for symmetrical values of order parameters across the grain boundaries. It should be noted that the grain boundary energy and thickness vary with the gradient energy penalty, κ .^[42]

The stored energy density term in the Equation (17), provides the driving force for microstructural evolution due to high dislocation density in deformed grains. This term can be approximated by the stress field of dislocations which are formed during the plastic deformation as^[1]

$$f_s = \frac{1}{2} \rho G b^2 \quad (19)$$

where ρ is the dislocation density field at each point, derived from the order parameters and their respective dislocation densities^[43] through the application of Moelans' interpolation function^[44,45]

$$\rho(\eta_1, \eta_2, \dots, \eta_g) = \frac{\sum_{i=1}^g \eta_i^2 \rho_g}{\sum_{j=1}^g \eta_j^2} \quad (20)$$

The dislocation density at each grid point, ρ_g , is obtained from the results of crystal plasticity simulations. For the purpose of comparative analysis with previous studies, ρ_g is considered to be uniform within each grain, with a random value assigned between $0.75\bar{\rho}$ and $1.25\bar{\rho}$, where $\bar{\rho}$ represents the average dislocation density.^[43]

The microstructural evolution equation can be obtained from nonconserved order parameters, based on the time-dependent Ginzburg–Landau equation,^[38] also known as the Allen–Cahn equation^[46]

$$\frac{\partial \eta_i(r, t)}{\partial t} = -L \frac{\delta \mathcal{F}}{\delta \eta_i(r, t)} \quad (21)$$

where L is the relaxation coefficient related to the interfacial mobility, t is time, and r is the spatial position of order parameters in the system. Now using the total free energy function (Equation (17)), the evolution equation of the system becomes^[43]

$$\frac{\partial \eta_i}{\partial t} = -L \left[m_0(-\eta_i + \eta_i^3 + 2\gamma \eta_i \sum_{j \neq i}^g \eta_j^2) - \kappa \nabla^2 \eta_i + G b^2 \frac{\eta_i}{\sum_{j=1}^g \eta_j^2} (\rho_g - \rho) \right] \quad i = 1, 2, \dots, g \quad (22)$$

In order to simulate the SRX kinetics, the set of kinetic equations (Equation (22)) have to be solved numerically using the

finite difference method by projecting the continuous system on a lattice of discrete points.^[38] The phase-field equations are also discretized, resulting in a set of algebraic equations. Solution of the algebraic equations yields the values of the phase-field variables in all lattice points.

A finite difference discretization technique using uniform lattice spacing, and with a central second-order stepping in space and forward stepping in time, is most widely used because of its simplicity

$$\frac{\partial \eta_i(r, t)}{\partial t} = \frac{\eta_i(r, t + \Delta t) - \eta_i(r, t)}{\Delta t} \quad (23)$$

where Δt is the time step for integration.

Active parameter tracking^[47,48] is utilized for computational efficiency. It should be pointed out that at every grid point only a few phase-field variables are nonzero and contribute to the evolution of the system. With a sparse data structure, the computations are simplified by iterating through only nonzero order parameters at any grid point. The list of active order parameters at each point is described as

$$\mathcal{P}(r, t) = \{(i, \eta_i) : \eta_i(r, t) > \varepsilon\} \quad (24)$$

where ε is chosen to be a small positive threshold value, wherein, only order parameters bigger than that are stored.

More importantly, IFN the value of any order parameter is zero at all points in a neighborhood, the value of the order parameter at center point will remain zero during the next time step. Therefore, an active parameter list should be considered in order to account for the possibility of an order parameter entering or leaving a point from neighboring points.

The following relations were derived for relating the simulation coefficients to the grain boundary energy, γ_{gb} , and grain boundary mobility, M_{gb} , as^[41]

$$\kappa = \frac{3}{4} \gamma_{\text{gb}} l_{\text{gb}} \quad (25)$$

$$L = \frac{4M_{\text{gb}}}{3l_{\text{gb}}} \quad (26)$$

$$m_0 = \frac{6\gamma_{\text{gb}}}{l_{\text{gb}}} \quad (27)$$

where l_{gb} is the grain boundary width which is a model parameter.

The boundary mobility for high angle grain boundaries (HAGB), $M_{\text{gb}}(m^4 J^{-1} s^{-1})$, is defined as^[49]

$$M_{\text{gb}} = M_0 \exp\left(\frac{-Q_g}{RT}\right) \quad (28)$$

where Q_g is the activation energy for the migration of a HAGB, R is the universal gas constant, and M_0 is the preexponential factor.

A 2D microstructure representative of IFN steel was simulated to study the SRX process under annealing at 750 °C. The parameters used for the simulation are listed in **Table 3**.

As noted earlier, the initial microstructure for the 2D simulation was derived from the results of the crystal plasticity

Table 3. Material properties of IFN steel on the phase-field model.

Q_g [kJ mol ⁻¹]	R [J mol ⁻¹ K ⁻¹]	M_0 [mol m j ⁻¹ s ⁻¹]	ϵ	γ_{gb} [J m ⁻²]	G [GPa]	B [Å]
140 ^[59]	8.314	0.43 ^[59]	10 ⁻⁶	0.79 ^[60]	69.2 ^[60]	2.48 ^[61]

simulation. The edges were then cropped, and the grid size increased to 1750 × 930. The grid spacing, Δx , was set to 0.543 μm, considering the scale of the original microstructure, the crystal plasticity simulation, and the phase-field grid. The grain boundary width, l_{gb} , was set to 4 Δx to ensure adequate numerical resolution across the diffuse interface. The simulation time step, Δt , was set to 1 × 10⁻² (s) to maintain numerical stability during simulation. Each grain is assigned a unique order parameter, as well as new recrystallized grains.

The evolution of the 2D microstructure is solved at each grid point using finite difference, with an eighth-order scheme for spatial derivatives and the Forward Euler method for time integration.

2.4.1. Grain Nucleation

The site-saturated nucleation assumption was adopted to model grain nucleation in the phase-field simulations. This assumption stipulates that all nucleation events are presumed to occur at the inception of recrystallization.

Experimental observations have indicated that, under conditions of uniform deformation, nucleation events are more likely to initiate at triple junctions and grain boundaries compared to the interior of grains.^[1] It has been hypothesized that triple junctions provide more energetically favorable nucleation sites due to their higher grain boundary area-to-volume ratio.^[50,51] Consequently, these assumptions will be incorporated in the present investigation.

Prior research^[43,52] has employed a probability-based algorithm for selecting seed positions by summing the normalized gradients of all order parameters at each grid point r , $\sum_{i=1}^g |\nabla \eta_i(r)|$. This approach identifies triple junctions as high-probability nucleation sites but assigns equal probability to all two-grain boundaries. In this article, we enhance this method by additionally considering the normalized gradient of total dislocation density at each

position, $|\nabla \rho_g(r)|$. This modification enables a more accurate prediction of nucleation site locations, especially on two-grain boundaries, rather than relying on random selection.

In prior research,^[43,53] the number density of nuclei was estimated from the experimentally determined average grain size at the completion of recrystallization. This approach relies on the assumption that the number of grains in the fully recrystallized microstructure is equal to the initial number of recrystallized nuclei. While this assumption is generally tenable, it necessitates experimental measurement of the final average grain size. In this article, a more direct approach is adopted by selecting the number of nuclei at each grid point based on a nucleation probability exceeding a threshold. This threshold is determined by the relative position of the average within the total dislocation density domain. This method obviates the need for experimental investigations.

To facilitate comparison, the simulation with constant dislocation density employed the same number of nuclei as the previous simulation, though their spatial distribution was randomized.

A circular nucleus, centered at the selected position, is introduced into the simulation domain. The initial order parameter within this nucleus is governed by the following function^[43]

$$\eta_i = \frac{1}{2} \left(1 - \tanh \left(\frac{d - r_{seed}}{2\Delta x} \right) \right) \quad (29)$$

where d represents the radial distance from the center of the nucleus and r_{seed} denotes the radius of the nucleus, which is fixed at 14 Δx in the present study. Subsequent to the insertion of nuclei into the phase-field domain, an initial hold period is implemented to allow the microstructure to accommodate the newly formed recrystallized grains.^[54] This approach mitigates the occurrence of unphysical behavior arising from overlapping order parameters.

It should be noted that the holding time is neglected in the total time of microstructural evolution.

3. Results and Discussions

Figure 5 depicts the IPF color map of the deformed microstructure, obtained through crystal plasticity simulations at an average

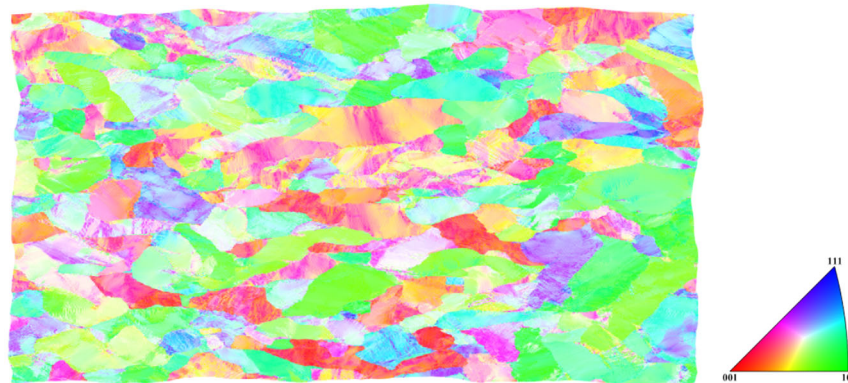


Figure 5. Final grain structure obtained from crystal plasticity simulation (IPF color map).

true von Mises strain of 0.45, based on the initial microstructure shown in Figure 3. The results indicate that the grains have elongated perpendicular to the compression axis. Additionally, significant changes in the crystallographic orientation of the original grains are evident.

Unfortunately, the DAMASK postprocessor does not calculate the deformed grain topology directly but provides the displacement vector field. The deformed microstructure topology was generated by vectorially displacing each grid point of the initial grain structure shown in Figure 3, according to the displacement field computed via crystal plasticity simulation. The state of the deformed microstructure was then utilized as the basis for initializing the order parameter field required for subsequent phase-field modeling.

It is well-established that the phase-field method inherently introduces a finite interface width. Consequently, the microstructure needs to establish a finite width at the grain interfaces, that is, the grain boundaries, to be used as the initial microstructure in the nucleation process and the subsequent SRX simulation.

To minimize spurious alterations in grain area during the construction of this diffuse interface, particularly critical for smaller grains, a refined spatial discretization was implemented. Specifically, the grid resolution was increased to ensure that the characteristic length scale of the diffuse interface was significantly smaller than the minimum grain size. This procedure is crucial to prevent the numerical dissolution of smaller grains, a phenomenon that arises when the interface width becomes comparable to or exceeds the grain dimensions.

To achieve this, a custom interpolation algorithm was developed to map the discrete grain topology data along with the total dislocation density distribution onto the refined computational grid. Subsequently, a unique order parameter field was generated for each grain such that the regions occupied by grains were assigned a value of 1, while the remaining regions were set to 0. This binary field represented the initial sharp interface condition. To initiate the diffuse interface formation, a brief temporal evolution of the order parameter field was performed according to Equation (22). This evolution was terminated upon attainment of a symmetric diffuse interface profile, ensuring a consistent representation of grain boundaries throughout the microstructure. **Figure 6** illustrates the processed microstructure, visualized using order parameters and Equation (30).^[27] As shown, the diffuse interfaces are accurately formed throughout the simulation domain.

$$\varphi(r, t) = \sum_{i=1}^g \eta_i^2(r, t) \quad (30)$$

The final step in the coupling process that involves extracting and interpolating the total dislocation density data from the crystal plasticity results onto the new grid. **Figure 7** illustrates the distribution of total dislocation density, overlaid with the grain boundaries. The DAMASK crystal plasticity simulation accurately captures the heterogeneous distribution of dislocation density and the accumulation of dislocations at grain boundaries during plastic deformation. This dislocation density distribution, coupled with the order parameters, serves as the initial conditions for the phase-field model, enabling

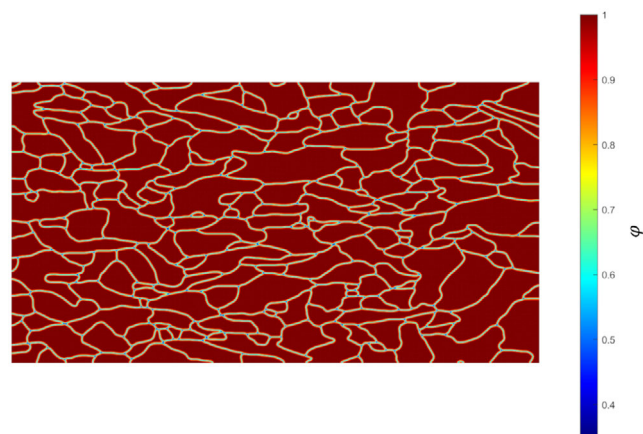


Figure 6. Grain topology of the microstructure resulting from crystal plasticity simulation showing diffuse interface development after holding time in phase-field model.

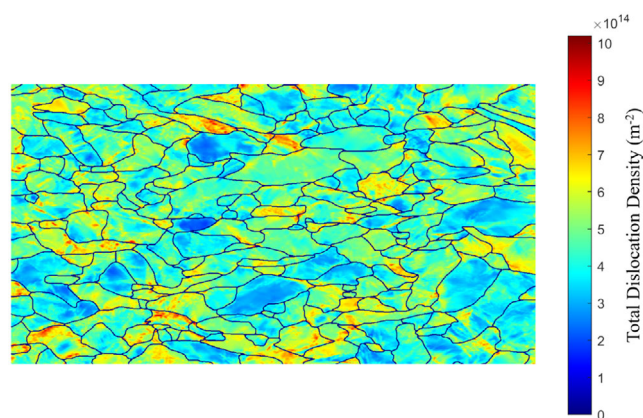


Figure 7. Distribution of total dislocation density, with overlaid grain boundaries.

the prediction of nucleation sites within the deformed microstructure.

As discussed previously, nucleation events are more likely to occur at triple junctions and grain boundaries than within the grain interiors. To identify potential nucleation sites, the gradients of all order parameters at each grid point were summed and normalized according to its maximum and minimum value. **Figure 8**(bottom) presents the normalized probability of nucleation at different positions within the microstructure. It is evident that triple junctions exhibit the highest nucleation probability, followed by two-grain boundaries, with the interior of grains having the lowest probability.

As previously discussed, in previous studies,^[39,43,53] the density of nuclei was determined experimentally, and nuclei were then randomly positioned in high-probability areas. In this article, we consider dislocation density gradients in addition to high-probability areas. **Figure 8**(top) shows the relative probability of nucleation, calculated by summing the high-probability areas from **Figure 8**(bottom) with the normalized gradient of the total dislocation density field at each grid point. This

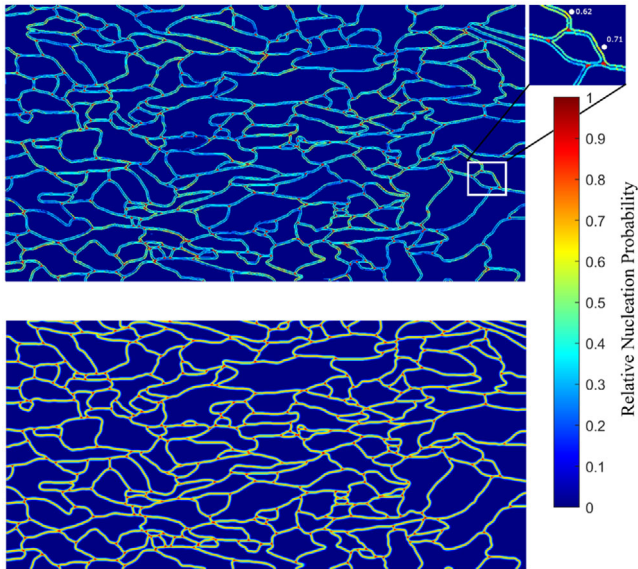


Figure 8. Normalized nucleation probability calculated from gradients of total dislocation density (top) and order parameters (bottom).

approach not only prioritizes triple junctions but also assigns different probabilities to two-grain boundaries. By selecting locations with a probability exceeding 0.59 (a threshold determined by the relative position of the average within the total dislocation density domain), the total number of nuclei and their positions within the simulation domain can be determined, eliminating the need for experimental investigations and random seed placement.

Once the total number of nuclei is determined, two sets of locations are selected: one based on the probabilities shown in Figure 8(top) and the other chosen randomly from the high-probability areas identified in Figure 8(bottom). A unique order parameter is then assigned to each nucleus using Equation (1). Subsequently, a nucleation holding time is implemented to allow the microstructure to accommodate the newly formed recrystallized grains. The two sets of order parameters can be compared with each other in two separate phase-field simulations.

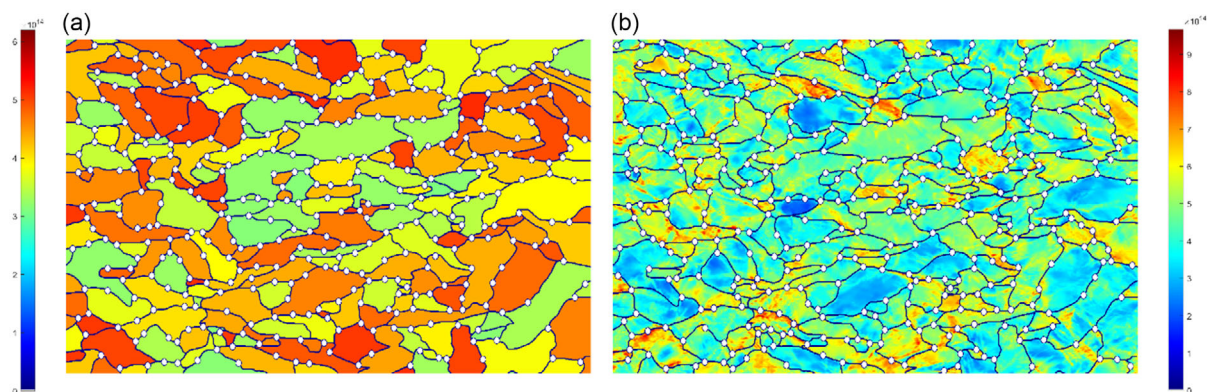


Figure 9. The seeded microstructure considering a) random nucleation and b) normalized nucleation probability calculated from gradients of total dislocation density. The color bar showing the total dislocation density (m^{-2}).

Figure 9 presents two variants of a seeded, deformed microstructure, each overlaid with contours of total dislocation density. To initiate the SRX process, 379 nuclei were incorporated into the microstructure via a stochastic algorithm. In the first configuration (Figure 9a), nuclei were deterministically positioned, while in the second (Figure 9b), their locations were randomized. It is evident that the nuclei exhibit a preference for sites of high dislocation density, such as triple junctions and grain boundaries. This seeded microstructure will be employed as the starting point for subsequent SRX phase-field simulations.

Figure 10 presents a series of microstructural snapshots, capturing the temporal evolution of the microstructure's topology. The color scale in the figure is indicative of dislocation density, while black regions delineate the grain boundaries. A side-by-side comparison of the two models reveals distinct microstructural evolution behaviors. The dislocation distribution model results in a more homogeneous distribution of recrystallized grains, with a relatively uniform growth rate. In contrast, the constant dislocation density model, with its stochastic nucleation, leads to a heterogeneous distribution of recrystallized grains. Regions with a high density of nuclei exhibit accelerated grain growth, while regions with fewer nuclei experience slower growth rates. The growth kinetics of individual grains in the constant dislocation density model appear to be influenced by the local dislocation density gradient.

Upon examining the final stages of recrystallization, significant differences emerge between the two models. The dislocation density distribution model results in a microstructure composed of relatively uniform and equiaxed grains, consistent with typical recrystallization behavior. In contrast, the constant dislocation density model leads to a microstructure with elongated grains. This disparity is likely due to the proximity of nucleation sites in the random seeding process.

The disparity in scale between the critical radius of recrystallized nuclei and the final recrystallized grain size presents a significant computational challenge. Given that the critical radius is substantially smaller than the final grain size, direct simulation of nuclei growth is computationally prohibitive unless the physical dimensions of the simulation domain are severely restricted,

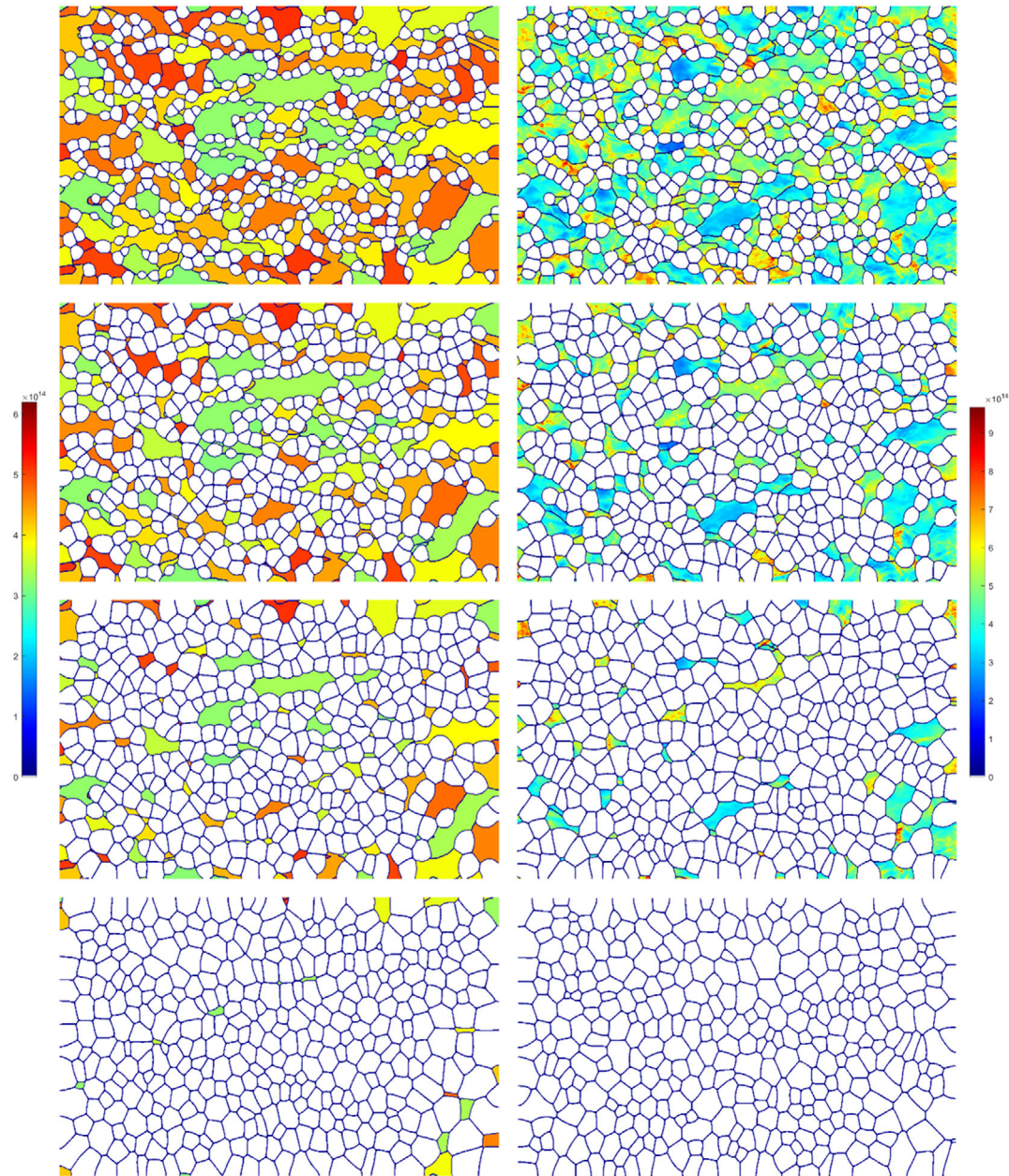


Figure 10. Simulated recrystallization microstructures at increasing times ($t = 122.7, 172.7, 222.7, 322.7$ s, top to bottom). Comparison of constant dislocation density model (left) and model with dislocation density distribution (right). The color bar showing the total dislocation density (m^{-2}) and the times are corrected.

which potentially compromising the representation of microstructural evolution at larger scales. Consequently, due to inherent resolution limitations of the phase-field model, it becomes computationally imperative to introduce recrystallization nuclei of a size sufficient for accurate representation within the discretized domain. Employing recrystallization seeds larger than the critical nucleus size represents a necessary deviation from physical reality for computational tractability. Consequently, the simulated recrystallization process is artificially advanced in time. To reconcile this discrepancy, a temporal correction, as described

below, is implemented to ensure that the simulated kinetics accurately reflect the physical processes.

To quantify the temporal duration required for a recrystallization nucleus to evolve from its critical radius to the artificially introduced seed radius, a series of independent simulations is conducted. Each simulation features a single recrystallization nucleus embedded within a distinct region of the deformed microstructure. This approach accounts for spatial variations in microstructural features that may influence growth kinetics. The growth velocity of the recrystallized

nucleus is subsequently determined by averaging the temporal evolution of the nucleus radius across these simulations. This averaged growth velocity, in conjunction with the known critical and seed radii, allows for the determination of the time interval required for growth from critical radius to the seed radius, effectively establishing the appropriate initial time offset for subsequent simulations. This offset corrects for the artificial advancement of the recrystallization process inherent in initializing the simulation with larger-than-critical nuclei. The critical radius itself, a key parameter in this analysis, can be estimated using the Bailey–Hirsch criterion,^[55] which exhibits a dependence on the dimensionality of the simulation domain.

$$r_{\text{BH}} = \frac{2(n_{\text{dim}} - 1)\gamma_{\text{gb}}}{\rho G b^2} \quad (31)$$

where r_{BH} is the critical radius of the recrystallized nuclei and n_{dim} is the number of dimensions in the simulation domain.

It is worth noting that the two models did not converge within the same simulation time (322.7 s). Experimental observations of the microstructure after 300 s of annealing (**Figure 11**) demonstrate that recrystallization is fully completed within this timeframe. Consequently, it can be inferred that the results obtained from the dislocation density distribution model provide compelling evidence for the validity of the proposed coupling approach.

Quantitative microstructural analysis revealed a grain count of 531, exceeding the predicted nucleation density of 379. However, when accounting for the previously established disparity in scale between the critical radius of recrystallized nuclei and the initial seed radius, a revised assessment of the predicted nucleation density demonstrates improved concordance with experimental observations. Specifically, by neglecting the small grains, the predicted value approaches the experimentally determined value, suggesting that the initial model, provides a reasonable approximation of the effective nucleation density contributing to the dominant microstructural features.

A comparison of the average grain size between the simulated (23.73 μm) and experimental microstructure (22.68 μm) reveals a difference of $\approx 4.62\%$. This relatively small discrepancy indicates a high degree of agreement between the simulated and experimental results, suggesting that the proposed coupling approach accurately captures the essential physics of recrystallization. It is

noteworthy that this level of agreement was achieved despite the fact that all material parameters were obtained from existing literature, highlighting the robustness of the proposed modeling framework.

Microstructural analysis of the model employing a constant dislocation density yielded an average grain size of 24.21 μm . While this value exhibits closer proximity to the experimentally determined grain size compared to alternative models, it is crucial to acknowledge that this value was determined at an equivalent simulation time as the model incorporating a dislocation density distribution. As previously established, recrystallization in the constant dislocation density model was incomplete at this time point. Extending the simulation duration until complete recrystallization is achieved would result in further grain growth, consequently, increasing the average grain size and exacerbating the deviation from the experimentally observed value.

The classical Johnson–Mehl–Avrami–Kolmogorov (JMAK) equation^[56–58] is a widely employed model for predicting the overall kinetics of primary recrystallization in deformed metals. The recrystallization fraction, X , is expressed as

$$X = 1 - \exp(-kt^n) \quad (32)$$

where t is the annealing time and k and n are Avrami coefficient and Avrami exponent. Based on the preceding discussion, SRX is approximated by a site saturation nucleation condition. Given that the SRX process simulation in this study is conducted on a 2D grid, the Avrami exponent is anticipated to be $n = 2$.

To quantify the recrystallization kinetics, the recrystallized fraction was determined by analyzing the area of recrystallized grains at various time steps for both the current model and the constant dislocation density model. These data are subsequently plotted in **Figure 12**. By fitting the JMAK equation to the MPF results, the Avrami parameters were extracted; these parameters are presented in Equation (33) for Model considering the dislocation density distribution and Equation (34) for Model with constant dislocation density. The Avrami exponent was found to be 2.02 ($R^2 = 0.9998$) for the current model and 1.95 ($R^2 = 0.9985$) for the constant dislocation density model. This indicates that the results of the proposed coupled model are in better agreement with the expected time exponent for

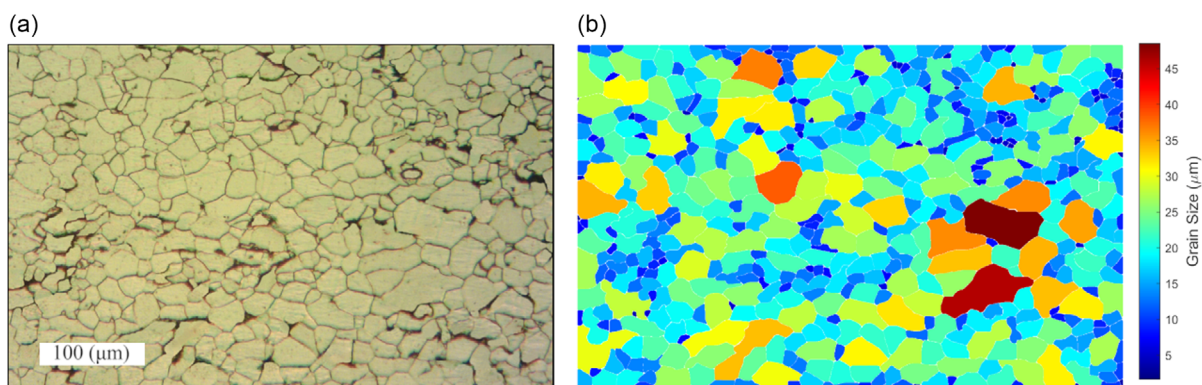


Figure 11. Microstructure of recrystallized IFN steel after 300 s annealing: a) experimental microstructure; and b) corresponding grain size distribution (color-coded).

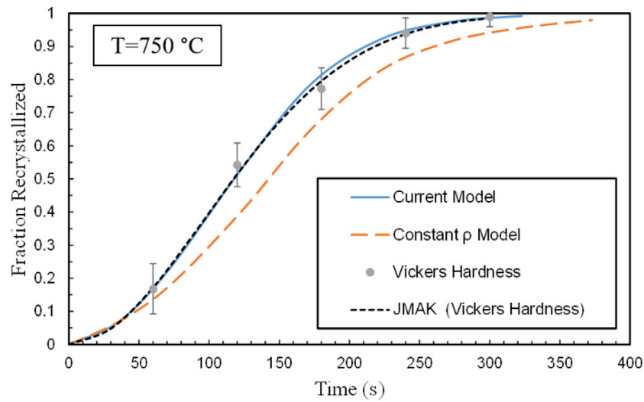


Figure 12. Area fraction recrystallized as a function of time: comparison of two simulation models and experimental results.

site-saturated nucleation and growth compared to the constant dislocation density model, thereby, confirming the consistency of the proposed model with SRX theory.

Furthermore, Figure 12 presents the experimentally determined fraction recrystallized, calculated from Vickers hardness measurements of IFN-steel samples annealed at 750 °C for varying durations. The Avrami parameters, fitted to experimental Vickers hardness results according to the JMAK equation (Equation (9)), are presented in Equation (35) and plotted in Figure 12.

$$X = 1 - \exp(-4.428 \times 10^{-5} t^{2.02}) \quad (33)$$

$$X = 1 - \exp(-4.566 \times 10^{-5} t^{1.95}) \quad (34)$$

$$X = 1 - \exp(-6.678 \times 10^{-5} t^{1.94}) \quad (35)$$

A comparison of the JMAK curve derived from experimental data and the curve generated from the current model reveals an excellent agreement. This strong correlation indicates that the proposed coupled model accurately predicts the nucleation density, nucleation site positions, and their temporal evolution during the recrystallization process.

Figure 13 presents grain size distributions obtained from experimental measurements and two phase-field simulations employing different approaches: the current model that considers

the total dislocation distribution and a constant dislocation density model. Comparison of the distributions reveals that the current model exhibits closer agreement with the experimental data. Both the experimental and current model distributions show a similar unimodal shape with a peak frequency around 15–20 μm. While the experimental distribution displays a slightly broader spread and a longer tail toward larger grain sizes, the current model captures the general trend and central tendency reasonably well. In contrast, the constant ρ model demonstrates a distinct distribution, with a sharper peak shifted towards smaller grain sizes around 10–15 μm and a less pronounced tail. This discrepancy indicates that the current model more accurately represents the underlying physical mechanisms governing grain growth compared to the constant dislocation density model, which underpredicts the average grain size and fails to capture the observed distribution shape.

4. Conclusions

In this article, a comprehensive computational framework was developed by coupling a physics-based crystal plasticity model with a MPF model to accurately simulate 2D SRX. The integration of the crystal plasticity model significantly enhances the representation of plastic deformation mechanisms, providing a more precise input for the phase-field model.

A robust coupling algorithm was implemented to extract the initial grain structure directly from optical microscopy images of the as-received microstructure. Subsequent crystal plasticity simulations were conducted, and the resulting deformed microstructure was then utilized as the initial condition for the phase-field model.

Leveraging the additional information provided by the crystal plasticity model, such as dislocation density distribution and deformed grain boundaries, the total number and positions of nucleation sites in the deformed microstructure were accurately determined.

To validate the proposed model, the simulation results were compared with experimental measurements and a conventional constant dislocation density model from the literature. The proposed model demonstrated exceptional agreement with experimental observations, significantly outperforming the conventional approach.

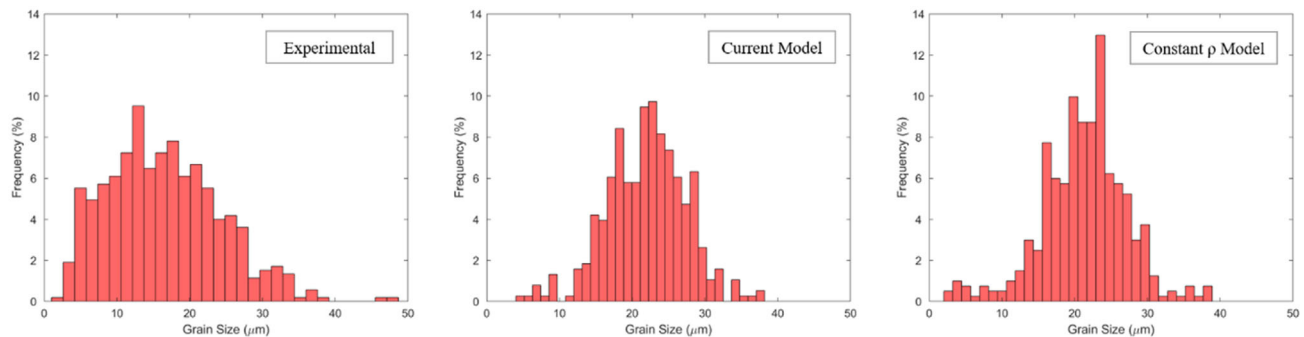


Figure 13. Grain size distributions for the fully recrystallized state predicted by two phase-field models (current and constant dislocation density), compared with experimental data.

The coupled crystal plasticity-phase-field model offers a reliable and accurate prediction of grain size distribution and evolution during the full SRX process in IFN steel, providing valuable insights into microstructure development.

Acknowledgements

Financial support by the office of the Research Council of Shiraz University through grant no. 99-GR-ENG 15 is appreciated.

Conflict of Interest

The authors declare no conflict of interest.

Author Contributions

Alireza Rezvani: conceptualization (equal); formal analysis (lead); investigation (lead); methodology (equal); software (lead); validation (equal); visualization (lead); writing—original draft (lead); writing—review and editing (equal). **Ramin Ebrahimi:** conceptualization (equal); funding acquisition (lead); methodology (equal); resources (lead); resources (lead); writing—review and editing (equal). **Ebad Bagherpour:** conceptualization (equal); funding acquisition (equal); writing—review and editing (equal).

Data Availability Statement

The data that support the findings of this study are available from the corresponding author upon reasonable request.

Keywords

compression test, crystal plasticity, interstitial free steel, phase-field, static recrystallization

Received: January 13, 2025

Revised: April 13, 2025

Published online:

- [1] J. Humphreys, G. S. Rohrer, A. Rollett, *Recrystallization And Related Annealing Phenomena*, 3rd Ed., (Eds: J. Humphreys, G.S. Rohrer, A. Rollett), Elsevier, Oxford **2017**, pp. 145–197.
- [2] K. Huang, K. Marthinsen, Q. Zhao, R. E. Logé, *Prog. Mater. Sci.* **2018**, *92*, 284.
- [3] F. J. Humphreys, M. Hatherly, *Recrystallization and Related Annealing Phenomena*, 2nd Ed., (Eds: F.J. Humphreys, M. Hatherly), Elsevier, Oxford **2004**, pp. 321–331.
- [4] H. Hallberg, *Metals* **2011**, *1*, 16.
- [5] P. Bate, M. F. Ashby, F. J. Humphreys, C. M. Sellar, H. R. Shercliff, M. J. Stowell, *Ser. A: Math., Phys. Eng. Sci.* **1999**, *357*, 1589.
- [6] D. Raabe, R. C. Becker, *Modell. Simul. Mater. Sci. Eng.* **2000**, *8*, 445.
- [7] T. Takaki, Y. Hisakuni, T. Hirouchi, A. Yamanaka, Y. Tomita, *Comput. Mater. Sci.* **2009**, *45*, 881.
- [8] T. Takaki, Y. Tomita, *Int. J. Mech. Sci.* **2010**, *52*, 320.
- [9] T. Takaki, A. Yamanaka, Y. Higa, Y. Tomita, *J. Comp-Aided Mater. Des.* **2007**, *14*, 75.
- [10] A. Vondrous, P. Bienger, S. Schreijäg, M. Selzer, D. Schneider, B. Nestler, D. Helm, R. Mönig, *Comput. Mech.* **2015**, *55*, 439.
- [11] K. M. Min, W. Jeong, S. H. Hong, C. A. Lee, P. R. Cha, H. N. Han, M. G. Lee, *Int. J. Plast.* **2020**, *127*, 102644.
- [12] K. M. Min, H. Lee, H.-D. Joo, H. N. Han, M.-G. Lee, *Int. J. Plast.* **2024**, *180*, 104049.
- [13] Q. Luan, J. Lee, J.-H. Zheng, C. Hopper, J. Jiang, *Comput. Mater. Sci.* **2020**, *173*, 109419.
- [14] A. M. Roy, S. Ganesan, P. Acar, R. Arróyave, V. Sundararaghavan, *Acta Mater.* **2024**, *266*, 119645.
- [15] R. Dierck, C. B. Richard, *Modell. Simul. Mater. Sci. Eng.* **2000**, *8*, 445.
- [16] D. Raabe, *Ann. Rev. Mater. Res.* **2002**, *32*, 53.
- [17] B. Radhakrishnan, G. Sarma, *JOM* **2004**, *56*, 55.
- [18] B. Radhakrishnan, G. Sarma, H. Weiland, P. Baggethun, *Modell. Simul. Mater. Sci. Eng.* **2000**, *8*, 737.
- [19] R. Doherty, D. Hughes, F. Humphreys, J. J. Jonas, D. J. Jensen, M. Kassner, W. King, T. McNelley, H. McQueen, A. Rollett, *Mater. Sci. Eng.: A* **1997**, *238*, 219.
- [20] D. Raabe, *J. Strain Anal. Eng. Des.* **2007**, *42*, 253.
- [21] M. Diehl, D. Wang, C. Liu, J. Rezaei Mianroodi, F. Han, D. Ma, P. J. Kok, F. Roters, P. Shanthraj, *Adv. Eng. Mater.* **2020**, *22*, 1901044.
- [22] F. Roters, M. Diehl, P. Shanthraj, P. Eisenlohr, C. Reuber, S. L. Wong, T. Maiti, A. Ebrahimi, T. Hochrainer, H. O. Fabritius, S. Nikolov, M. Friák, N. Fujita, N. Grilli, K. G. F. Janssens, N. Jia, P. J. J. Kok, D. Ma, F. Meier, E. Werner, M. Stricker, D. Weygand, D. Raabe, *Comput. Mater. Sci.* **2019**, *158*, 420.
- [23] F. Roters, P. Eisenlohr, L. Hantcherli, D. D. Tjahjanto, T. R. Bieler, D. Raabe, *Acta Mater.* **2010**, *58*, 1152.
- [24] L.-Q. Chen, *Scr. Metall. Mater.* **1995**, *32*, 115.
- [25] L.-Q. Chen, *Ann. Rev. Mater. Res.* **2002**, *32*, 113.
- [26] L.-Q. Chen, W. Yang, *Phys. Rev. B* **1994**, *50*, 15752.
- [27] D. Fan, L. Q. Chen, *Acta Mater.* **1997**, *45*, 611.
- [28] M. A. Groeber, M. A. Jackson, *Integr. Mater. Manuf. Innovation* **2014**, *3*, 56.
- [29] A. Ma, F. Roters, *Acta Mater.* **2004**, *52*, 3603.
- [30] A. Ma, F. Roters, D. Raabe, *Acta Mater.* **2006**, *54*, 2169.
- [31] E. Orowan, *Zeitschrift für Physik* **1934**, *89*, 634.
- [32] A. V. Amirkhizi, S. Nemat-Nasser, *Int. J. Plast.* **2007**, *23*, 1918.
- [33] S. Nemat-Nasser, T. Okinaka, L. Ni, *J. Mech. Phys. Solids* **1998**, *46*, 1009.
- [34] U. F. Kocks, A. S. Argon, M. F. Ashby, *Thermodynamics and Kinetics of Slip*, Vol. 19, Pergamon Press, Oxford **1975**.
- [35] W. Blum, P. Eisenlohr, *Mater. Sci. Eng.: A* **2009**, *510*, 7.
- [36] K. Sedighiani, M. Diehl, K. Traka, F. Roters, J. Sietsma, D. Raabe, *Int. J. Plast.* **2020**, *134*, 102779.
- [37] K. Sedighiani, K. Traka, F. Roters, D. Raabe, J. Sietsma, M. Diehl, *Mech. Mater.* **2022**, *164*, 104117.
- [38] N. Moelans, B. Blanpain, P. Wollants, *Calphad* **2008**, *32*, 268.
- [39] S. P. Gentry, K. Thornton, *IOP Conf. Ser.: Mater. Sci. Eng.* **2015**, *89*, 012024.
- [40] T. Takaki, T. Hirouchi, Y. Hisakuni, A. Yamanaka, Y. Tomita, *Mater. Trans.* **2008**, *49*, 2559.
- [41] N. Moelans, B. Blanpain, P. Wollants, *Phys. Rev. B* **2008**, *78*, 024113.
- [42] N. Moelans, B. Blanpain, P. Wollants, *Phys. Rev. Lett.* **2008**, *101*, 025502.
- [43] S. P. Gentry, K. Thornton, *Modell. Simul. Mater. Sci. Eng.* **2020**, *28*, 065002.
- [44] N. Moelans, *Acta Mater.* **2011**, *59*, 1077.
- [45] N. Moelans, A. Godfrey, Y. Zhang, D. Juul Jensen, *Phys. Rev. B* **2013**, *88*, 054103.
- [46] S. M. Allen, J. W. Cahn, *Acta Metall.* **1979**, *27*, 1085.
- [47] J. Gruber, N. Ma, Y. Wang, A. D. Rollett, G. S. Rohrer, *Modell. Simul. Mater. Sci. Eng.* **2006**, *14*, 1189.
- [48] S. Vedantam, B. S. V. Patnaik, *Phys. Rev. E* **2006**, *73*, 016703.
- [49] D. Turnbull, *JOM* **1951**, *3*, 661.
- [50] P. J. Clemm, J. C. Fisher, *Acta Metall.* **1955**, *3*, 70.
- [51] G. L. Wu, D. Juul Jensen, *Acta Mater.* **2007**, *55*, 4955.

- [52] B. Scholtes, R. Boulais-Sinou, A. Settefrati, D. Pino Muñoz, I. Poitroult, A. Montouchet, N. Bozzolo, M. Bernacki, *Comput. Mater. Sci.* **2016**, 122, 57.
- [53] Z. Aretxabaleta, B. Pereda, B. López, *Metall. Mater. Trans. A* **2014**, 45, 934.
- [54] A. M. Jokisaari, C. Permann, K. Thornton, *Comput. Mater. Sci.* **2016**, 112, 128.
- [55] J. E. Bailey, P. B. Hirsch, *Ser. A: Math. Phys. Sci.* **1962**, 267, 11.
- [56] M. Avrami, *J. Chem. Phys.* **1939**, 7, 1103.
- [57] M. Avrami, *J. Chem. Phys.* **1940**, 8, 212.
- [58] W. A. Johnson, *Trans. Trans. Am. Inst. Min. Metall. Eng.* **1939**, 135, 416.
- [59] M. Hillert, L. Höglund, *Scr. Mater.* **2006**, 54, 1259.
- [60] D. Raabe, L. Hantcherli, *Comput. Mater. Sci.* **2005**, 34, 299.
- [61] H. J. Frost, M. F. Ashby, *Deformation-Mechanism Maps: The Plasticity And Creep Of Metals And Ceramics*, Franklin Book Company Incorporated, Pergamon Press, Oxford **1982**.